International Journal of Fatigue 197 (2025) 108955



Contents lists available at ScienceDirect

International Journal of Fatigue

journal homepage: www.elsevier.com/locate/ijfatigue





Fatigue strength prediction of 410NiMo stainless steel with surrogate weld discontinuities

C. Constantineau [a], P.A. Deschênes [b], R. Dubois [b], M. Brochu [a,*]

[a] Department of Mechanical Engineering, Polytechnique Montréal, 2500 ch. de Polytechnique, Montréal H3T 1J4, Canada
[b] Institut de Recherche d'Hydro-Québec (IREQ), 1800 boul. Lionel-Boulet, Varennes, Québec J3X 1S1, Canada

ARTICLE INFO

Keywords:
3D models
CT scan
Martensitic stainless steel
Welded joints
Fatigue resistance
Finite element analysis
Hydraulic turbines

ABSTRACT

The fatigue strength of martensitic stainless steel 410NiMo, featuring slag-type discontinuities, was investigated to evaluate the accuracy of fatigue strength prediction models. This study examines the influence of volumetric discontinuities introduced through robotic FCAW on fatigue strength, characterized using advanced techniques. High-resolution CT scanning (20 μm/voxel) enabled precise 3D modelling of the welded zones, supporting finite element simulations of the stress field. These simulations revealed complex distributions, with singularity exponents ranging from 0.27 to 0.45, lower than the typical 0.50 exponent associated with cracks. Fatigue experiments demonstrated that Linear Elastic Notch Mechanics (LENM), applied for the first time in this context, overestimated fatigue resistance by 34 %, whereas Linear Elastic Fracture Mechanics (LEFM), based on maximum discontinuity width, provided more accurate and conservative predictions, with an average deviation of 16 %. Fractographic analyses identified crack initiation sites at flux-filled micro-notches undetectable by CT resolution, while foreign elements from flux residues were observed, suggesting a potential embrittlement effect. These findings indicate that large, rounded discontinuities in welds can behave like cracks due to embedded microscopic cracks or notches. The study highlights the limitations of LENM for volumetric discontinuities in FCAW welds and establishes a framework for improving fatigue strength prediction.

1. Introduction

1.1. Context of research

Hydraulic turbines are essential for renewable energy generation. Their durability directly affects the maintenance costs and the capacity to produce green energy during peak demand periods, such as winter mornings. Observations indicate that turbines within Hydro-Québec's network frequently surpass their initially expected service lifetime of 70 years. Achieving an operational service lifetime of 80 years requires advancements in the accuracy of fatigue life predictions.

Stainless steel 13Cr-4Ni components, joined with 410NiMo, is commonly used in hydraulic turbine manufacturing, particularly for the crowns, bands and blades of Francis turbines operated by Hydro-Québec. Some installations are designed to accommodate large-scale runners, with diameters reaching up to 10 m. Welding discontinuities, such as slag inclusions and lack of fusion, affect the material resistance to fatigue and must be considered to assess the fatigue life of the turbine and schedule appropriate servicing intervals.

Among these welding discontinuities, spherical oxide inclusions containing zirconium, silicon and aluminum have been identified [1,2]. D'Andrea et al. [3] further analyzed defects in 410NiMo multi-pass welds, revealing that the defect population consists of both spherical and elongated discontinuities, significantly influencing fatigue strength. Slag inclusions are another common critical flaw associated with flux-cored arc welding (FCAW). They form as a residue of molten flux resulting from incomplete interpass cleaning. These discontinuities form elongated wormlike shapes, as demonstrated by Boukani et al. [4], who investigates 410NiMo welds through several non-destructive tests (NDT) on T-shaped joints in hydraulic turbine runners. Hydro-Québec does not systematically remove these large discontinuities that are accounted as crack-like defect in fatigue strength predictions. Building on these findings, the present study investigates the fatigue strength of martensitic stainless steel 410NiMo by surrogating (intentionally introducing) volumetric discontinuities that mimic those observed in industrial conditions.

* Corresponding author.
E-mail address: myriam.brochu@polymtl.ca (M. Brochu).

https://doi.org/10.1016/j.ijfatigue.2025.108955
Received 28 January 2025; Received in revised form 13 March 2025; Accepted 23 March 2025
Available online 24 March 2025
0142-1123/© 2025 The Authors. Published by Elsevier Ltd. This is an open access article under the CC BY-NC license (http://creativecommons.org/licenses/by-nc/4.0/).

Nomenclature

AL	Atzori-Lazzarin
ASME	American Society of Mechanical Engineers
ASTM	American Society for Testing and Materials
AWS	American Welding Society
BSE	Backscattered electron
CMM	Columnar martensitic microstructure
CT	Computed-assisted tomography
EDS	Energy-dispersive spectroscopy
FCAW	Flux-cored arc welding
FEA	Finite element analysis
FGMM	Fine-grained martensitic microstructure
GDOES	Glow discharge optical emission spectroscopy
IIW	International institute of welding
KT	Kitagawa-Takahashi
LEFM	Linear elastic fracture mechanics
LENM	Linear elastic notch mechanics
MAPE	Mean absolute percentage error
NDT	Non-destructive testing
NSIF	Notch stress intensity factor
PM	Point method
PWHT	Post-weld heat treatment
RSD	Relative standard deviation
SEM	Scanning electron microscope
a	Discontinuity size
a_0	Transition point from short to long cracks in KT diagram
$a_{0,n}$	Transition point from short to long notches in AL diagram
a^*_n	Transition point from stress distribution to peak stress zone in AL diagram
e_f	Elongation to fracture
H	Specimens height
k_t	Stress concentration factor
N	Number of load cycles
N_f	Number of load cycles at failure
n	Number of load steps
R	Cyclic load ratio
t	Specimens thickness
W	Specimens width
x	Distance from the notch tip
Y	Geometrical factor
α	Singularity exponent
β	Dimensionless parameter dependent on the notch opening angle
ΔK_{th}	Threshold stress intensity factor range for long cracks
$\Delta K_{\text{th,n}}$	Threshold stress intensity factor range for notches
$\Delta\sigma$	Stress variation
$\Delta(\Delta\sigma)$	Increment in stress variation
$\Delta\sigma_i$	Stress variation at load step i
$\Delta\sigma_0$	Fatigue strength of specimens without defects
φ	Notch opening angle
ρ	Notch tip radius
σ_{nominal}	Nominal stress
σ_{UTS}	Ultimate tensile strength
σ_y	Yield strength
σ_{yy}	Local stress in Y direction
$\sigma_{yy(\max)}$	Maximum local stress in Y direction

1.2. Current approaches and limitations

Hydro-Québec's (H-Q) current approach to predict the operational fatigue life of hydraulic turbines containing discontinuities is based on linear elastic fracture mechanics (LEFM) [5,6]. After conducting non-destructive testing (NDT) by ultrasonic inspection, a Kitagawa-Takahashi diagram [7] is used to predict the fatigue strength (for a given life) of the 410NiMo welded material. This conservative approach may underestimate the material's fatigue resistance, potentially leading to designs with thicker joints that could impair the hydraulic performance of the assembly. This concern is supported by the thesis of Meimandi [8], which shows that the fatigue life of stainless steel 13Cr-4Ni is significantly affected by discontinuity sizes ranging from 0.25 mm to 1.62 mm. Consequently, Akbarian [9] investigated the fatigue strength of 410NiMo weld metal, developing a generalized Atzori-Lazzarin model [10,11] for welded fatigue specimens containing small, semi-spherical, artificial discontinuities. Additionally, Ghafoori-Ahangar et al. [12] studied fatigue behavior in 410NiMo welds, demonstrating that the Notch Stress Intensity Factor (NSIF) approach accurately predicts the fatigue strength of weld roots for various weld penetration depths. However, these studies primarily focused on geometrical features of welds and notch effects in 410NiMo weld metal, without addressing the influence of volumetric discontinuities, such as slag inclusions, which are commonly found in FCAW welds.

The NSIF has been extensively studied as a tool for understanding fatigue strength in notch components. NSIF has been applied to strictly defined V- and U-shaped notch opening angles, primarily for filet welds, as explored by Atzori and others [13–15]. These studies have established a strong foundation for using NSIF to predict fatigue strength in simplified geometries with well-defined stress fields.

More recently, Schuscha et al. [16] expanded the application of the NSIF to complex geometries, analyzing the effect of artificially generated shrinkage cavities on the fatigue strength of cast steel G21Mn5. This demonstrated the potential of NSIF to evaluate fatigue strength in components with irregular discontinuities. Furthermore, Consonni et al. [17] proposed a methodology for using surrogate slag inclusion discontinuities created with electrode coating residues to replicate realistic welding discontinuities.

While these contributions advanced the field, the application of NSIF to welded joints containing surrogate slag-type discontinuities in materials critical to hydroelectric turbine performance, such as 410NiMo, remains largely unexplored.

1.3. Novelty and objectives

This research addresses these gaps by combining experimental introduction of discontinuities, advanced characterization techniques, and fatigue strength prediction, bridging the divide between theoretical NSIF applications and real-world welded components with discontinuities.

The study provides novel contributions to the field by:

- **Application to 410NiMo weld metal**: A material essential for hydroelectric turbine performance yet insufficiently studied in terms of fatigue behavior with realistic discontinuities.
- **Controlled introduction of complex discontinuities**: Realistic slag inclusions, replicating critical flaws commonly associated with the FCAW process, are introduced into welded joints. These discontinuities are created using robotic welding, marking a pioneering approach for producing representative flaws under controlled and repeatable conditions. This enables controlled experiments that closely mimic real-world welding imperfections.
- **Advanced characterization and modelling**: Discontinuities are precisely characterized by CT scan, enabling highly detailed finite element analysis (FEA) of stress distributions.

- **Validation of NSIF applicability for complex discontinuities**: The study systematically evaluates the NSIF for discontinuities with varied stress distributions, extending its application beyond traditional notch geometries.

This research builds on prior studies but goes beyond their scope by addressing the unique challenges of fatigue strength evaluation in welded joints with surrogate discontinuities. Unlike studies limited to idealized notch geometries or shrinkage cavities, this work combines experimentally controlled discontinuities, advanced characterization, and NSIF validation to deliver practical insights into real-world welded joint behavior. The novel integration of robotic welding to introduce representative discontinuities provides an unprecedented framework for assessing fatigue resistance in critical hydroelectric turbine components.

1.4. Paper outline

The general objective of this work is to apply the generalized Atzori-Lazzarin approach using the linear elastic notch mechanics (LENM) to larger discontinuities having a wide range of geometries. The experimental approach in **Section 2** includes a detailed description of the sample manufacturing, the material characterization methods, the 3D discontinuity modelling using the CT scan, and the finite element simulation of the stress distribution around discontinuities. **Section 3** presents the results, beginning with welding and material characterization around the discontinuity, followed by finite element and experimental fatigue results, and further explains these findings through fractographic and chemical analyses. **Section 4** focuses on presenting predictions for fatigue strength using the LENM and LEFM approaches. **Section 5** provides a detailed discussion of these results. The conclusion of the analysis and the limitations of the current research are discussed in **Section 6**.

2. Material and methods

2.1. Material and specimens preparation

A 457.2 mm long plate made of S41500 steel was milled to create a U-groove cavity with a flat bottom. The surface was prepared by numerical machining. A 410NiMo filler metal was deposited using a flux-cored arc welding (FCAW) operation performed by a *SCOMPI*® welding robot developed by Hydro-Québec. During the entire welding operation, the plate temperature was maintained between 100 °C and 200 °C to reduce the cooling rate. The temperature range was controlled using thermocouples, ensuring consistent thermal conditions throughout welding. To facilitate the introduction of flux residue, a valley was intentionally formed between two weld beads as shown in Fig. 1. Flux residues were distributed along the weld root to obtain discontinuities with dimensions similar to those detected in industrial manufacturing conditions.

The flux residues were then covered by multiple weld beads and the excess material was grinded. The same process was performed on the other side of the plate which resulted in a fully penetrated weld of approximately 50 mm in width. A post-weld heat treatment (PWHT) was carried out at 605 °C for a period of 8 h and the part was cooled by ambient air. As demonstrated by Trudel et al. [18], PWHT at 600 °C for 2 h was shown to significantly reduce residual stresses. The sketches of weld bead deposition are presented in Fig. S.1 **of** Appendix A – **Supplementary Information**, which is available in the **supplementary section**.

Table 1 shows the chemical composition of the E410NiMo electrode used to manufacture the specimens and the nominal standard specifications of the AWS A5.22 M standard [19]. The bulk chemical analysis of the deposited filler metal was performed by glow discharge optical emission spectroscopy (GDOES) while the carbon and sulfur content were obtained by oxygen stream combustion-infrared absorption analysis [9].

Table 2 reports the results of a chemical analysis performed by Yoon et al. [20] on the cross section of a E electrode (K308LT, AWS A5.22 E308LT1-1/4, KSD 3612, Koryeo Rod, Korea) considered comparable to the electrode used in this study. Their analysis, performed by scanning electron microscopy (SEM) coupled with energy-dispersive spectroscopy (EDS), revealed the presence of silicon, titanium and zirconium, in the inner flux of the wire.

Three tensile tests were conducted by Akbarian [9] on specimens post-weld heat treated at 605 °C for 8 h. The average mechanical properties and standard deviation are presented in Table 3. The average tensile strength value is above the minimum required by AWS A5.22 M while the average elongation at break falls below the requirement. The presence of discontinuities in the weld could explain the low elongation value.

Following the PWHT, 15 fatigue specimens were machined in the transverse direction of the plate, allowing the discontinuity to pass through the reduced sections of the specimens. Fig. 2 shows the specimen cutting pattern and gives the dimensions of the fatigue specimens designed according to ASTM E466 specifications [21]. The blue contour indicates the position of a metallographic sample extracted from the weld extremity.

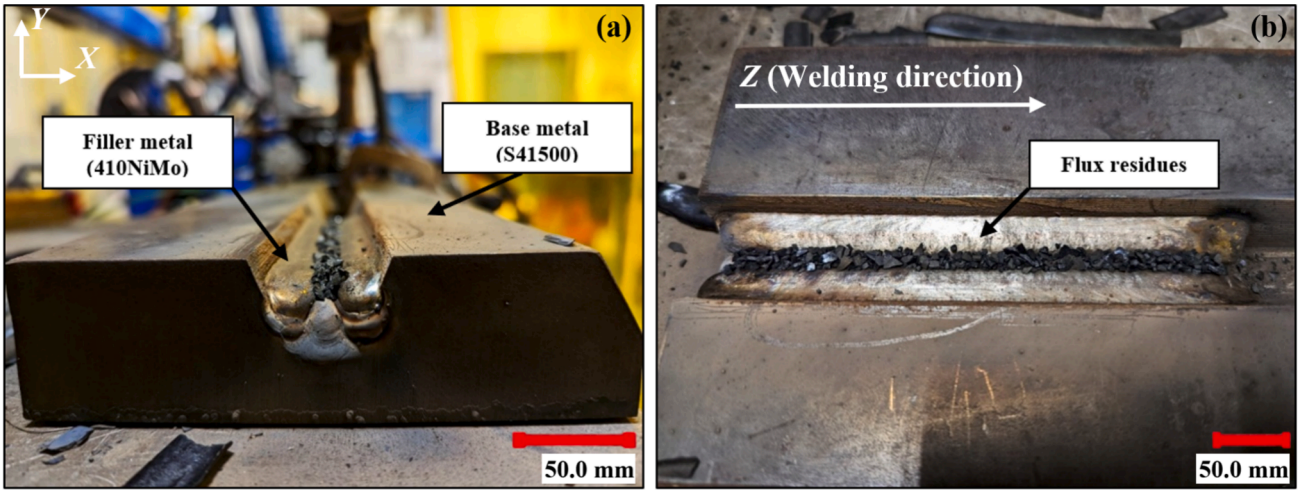


Fig. 1. Deposits of flux residues along the longitudinal axis of the welded plate: (a) Front view (b) Top view. Courtesy of Hydro-Quebec Research Institute (IREQ) technician René Dubois.

Table 1
Measured and nominal chemical compositions (wt.%) of 410NiMo filler metal.

Classification	C	Mn	P	S	Si	Cr	Ni	Mo
ER410NiMo [9]	0.025	0.34	0.018	0.009	0.5	11.7	5.32	0.66
E410NiMo (AWS A5.22M)	<0.06	<1.0	<0.04	<0.03	<1.0	11.0–12.5	4.0–5.0	0.4–0.7

Table 2
Chemical composition (wt.%) of the flux-cored wire [20].

Element	Fe	Cr	Si	Mn	Zr	Ti	Ni	K	Al
Wt.%	31.33	20.28	12.53	8.34	8.10	7.82	5.95	2.93	2.72

Table 3
Measured and nominal mechanical properties of the weld 410NiMo.

Classification	Yield stress at 0.2 % (σ_y)[MPa]	Ultimate tensile strength (σ_{UTS})[MPa]	Elongation to fracture (e_f)[%]
E410NiMo – HT [9]	680 ± 20	825 ± 22	11 ± 2.5
E410NiMo – HT (AWS A5.22M)	–	>760	>15

The external surfaces of all fatigue specimens were polished with SiC papers down to 1200 grit followed by a final polishing with diamond suspension of 9 μm and 1 μm.

2.2. Microstructural characterization around the discontinuity

The metallographic sample underwent the same polishing procedure used to prepare the fatigue specimens. A Villela reagent (1 g picric acid + 5 ml hydrochloric acid + 100 ml ethanol) applied for 30 s, according to the ASTM E407 standards [22], provided a good contrast of the martensitic microstructure.

One fatigue test was interrupted before failure to allow for metallographic observations aimed at identifying the location of the crack initiation site. A 9 mm sample was cut around the discontinuity in the reduced section and prepared as previously described. Approximately 1 mm of material was removed in the welding direction.

2.3. 3D geometric modelling of discontinuities

The geometry of 15 specific discontinuities was scanned from computer-assisted tomography (CT) and exported to ABAQUS CAE software for modelling. Fig. 3 shows an overview of the process steps performed to generate 3D geometric models from CT scans. Information about each processing step is provided in the subsections, and the characterization of two fatigue specimens is given as an example.

2.3.1. CT scan characterization

The discontinuity that traverses each specimen was characterized by Computed Tomography (CT) scans using a Shimadzu inspeXio SMX-225CT FPD HR Plus. The element size of the voxelized discontinuities

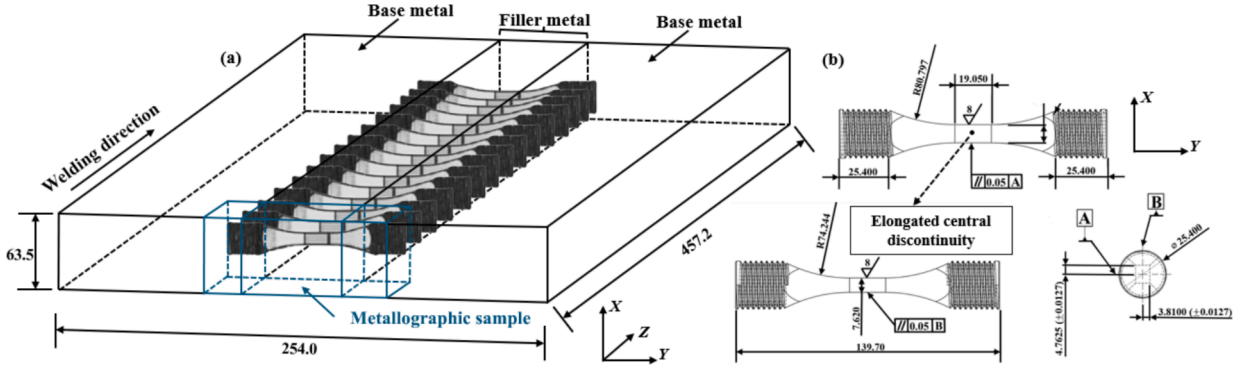


Fig. 2. Schematic of (a) The specimen cutting pattern in the weld plate and (b) The fatigue specimen dimensions, indicating the position of the elongated central discontinuity (all dimensions are in mm).

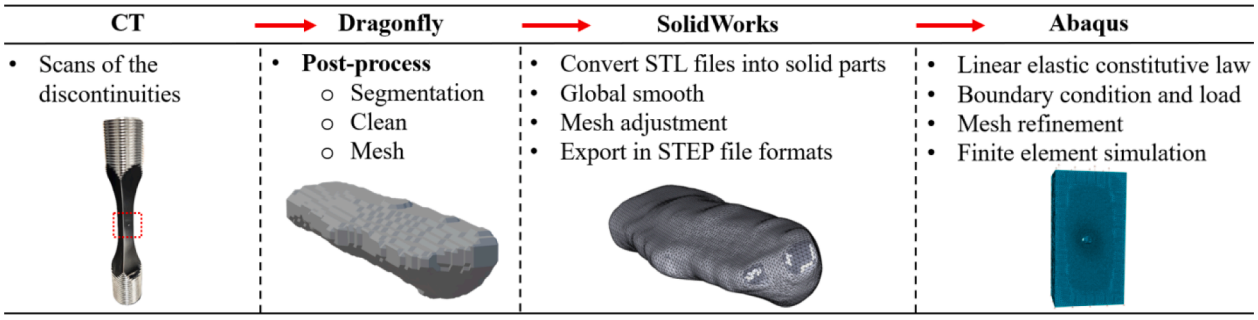


Fig. 3. Process flow: From CT scan post-processing in Dragonfly software to SolidWorks 3D CAD and ABAQUS CAE.

varied from 100 μm to 20 μm, with the maximum scan resolution being 20 μm per voxel. Dragonfly software was used to post-process the 3D scan data, involving segmentation, cleaning and meshing operations. The models of the discontinuities were imported in the SolidWorks 3D CAD software to smooth the global mesh surface and locally adjust the mesh using the ScanTo3D – Mesh Prep Wizard tool (see Fig. 4). The main purpose of using SolidWorks is to convert mesh-based formats (STL) obtained from Dragonfly software to feature-based formats (STEP). The conversion ensures compatibility when importing the volumetric model into ABAQUS CAE.

2.3.2. 3D geometric modelling of specimens

The 3D geometry of each discontinuity was incorporated into a prismatic volume that mimics the fatigue specimen's geometry and dimensions. The resulting model, shown in Fig. 5**(a) and (c)**, was compared to the transverse surface of the fatigue specimens (Fig. 5**(b) and (d)**) to validate the geometry and alignment. The smearing produced during the machining of the fatigue specimens was not considered in the 3D model.

2.3.3. Finite element model

The 3D geometric models were imported into ABAQUS CAE software to simulate the stress distribution around the discontinuities using finite element analysis (FEA). The material was modelled with elastic behavior characterized by a Young's modulus of 200 GPa and a Poisson's ratio of 0.3. The models were meshed using 10-node tetrahedral elements (C3D10). A coarse mesh with a resolution of 200 μm was applied to the bulk of the models, while a finer mesh with a resolution as small as 18 μm was used around the specimen discontinuities to precisely characterize the elastic stress distribution. A nominal stress (σ_{nominal}) of 1 MPa was applied, with a boundary condition of $U_{yy} = 0$ (no displacement in Y direction). The finite element simulation of specimen No.1, presented in Fig. 6, is provided as an example.

To ensure the accuracy and reliability of the finite element (FE) simulations, an incremental mesh refinement method was implemented. This approach involved increasing the number of elements by at least 20 % between each FE simulation, with convergence assessed by a maximum difference of 2 % in $\sigma_{yy(\max)}$ between simulations.

2.4. Fatigue tests

Fatigue testing was performed using the step-loading method first proposed by L. Locati in 1955 [23], and the results were analyzed using the simplified equation introduced by Maxwell et al. [24] to characterize the fatigue strength at $2E^6$ cycles. At each load step, if the specimen completed $2E^6$ cycles without fracture, the stress variation was incremented by 40 MPa. This incrementation process was repeated until failure occurred. One specimen (No.8) underwent a different treatment where the stress variation was incremented by 20 MPa.

The fatigue strength for $2E^6$ cycles was determined by evaluating the number of cycles at the failure step (N_f), along with the incremented stress variation ($\Delta(\Delta\sigma)$) and the stress variation at the step prior to failure ($\Delta\sigma_{(n-1)}$). It was calculated using the following equation:

$$\Delta\sigma = \Delta\sigma_{(n-1)} + \Delta(\Delta\sigma)\left(\frac{N_f}{2E^6}\right) \tag{1}$$

Fatigue tests were carried out on a Vibrophore 200 HFP 5100 at a stress ratio of $R = 0.1$ and a frequency of 108 Hz. The first stress level ($\Delta\sigma_1$) was independently selected for each fatigue specimen based on the FEA. The minimum fatigue strength of a specimen was estimated by dividing the fatigue strength of a 410NiMo reported for a smooth specimen at $R = 0.1$ and $2E^6$ cycles ($\Delta\sigma_0 = 520$ MPa [9]) by the stress concentration factor, k_t, specific to the discontinuity in the specimen. The resulting value was reduced by at least 40 MPa to avoid fatigue failure at the first load step.

3. Results

3.1. Weld and discontinuity characterization

Fig. 7 shows the martensitic microstructure of 410NiMo filler metal in the weld. Fig. 7**(a)** is the raw image, while annotations were added in Fig. 7**(b).** The grains clearly show the weld beads contours, characterized by alternating regions of columnar (CMM) and fine-grained martensitic microstructure (FGMM). The weld consists of a total of 44 beads, with a quasi-circular cross-section of the discontinuity visible in the middle. The microstructure around the discontinuity is consistent, with regions of CMM and FGMM arranged in the direction of heat extraction. Weld beads preceding the introduced discontinuity are referred to as the weld root, whereas those following the discontinuity are identified as the weld covering zone.

3.2. Finite element analysis

Fig. 8 shows, for the two specimens previously described in the methodology, the fracture surfaces (Fig. 8**(a) and (c)**) and the results of

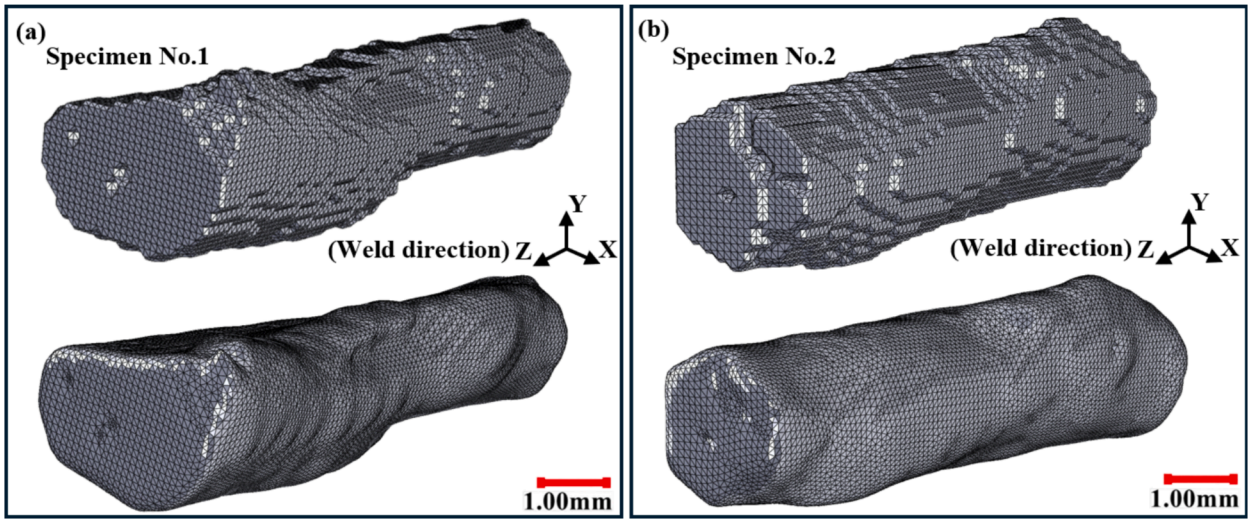


Fig. 4. Mesh models of discontinuities in welded specimens derived from CT scans and refined in SolidWorks software of (a) Specimen No.1 and (b) Specimen No.2. Rough mesh (top) and smoothed mesh (bottom).

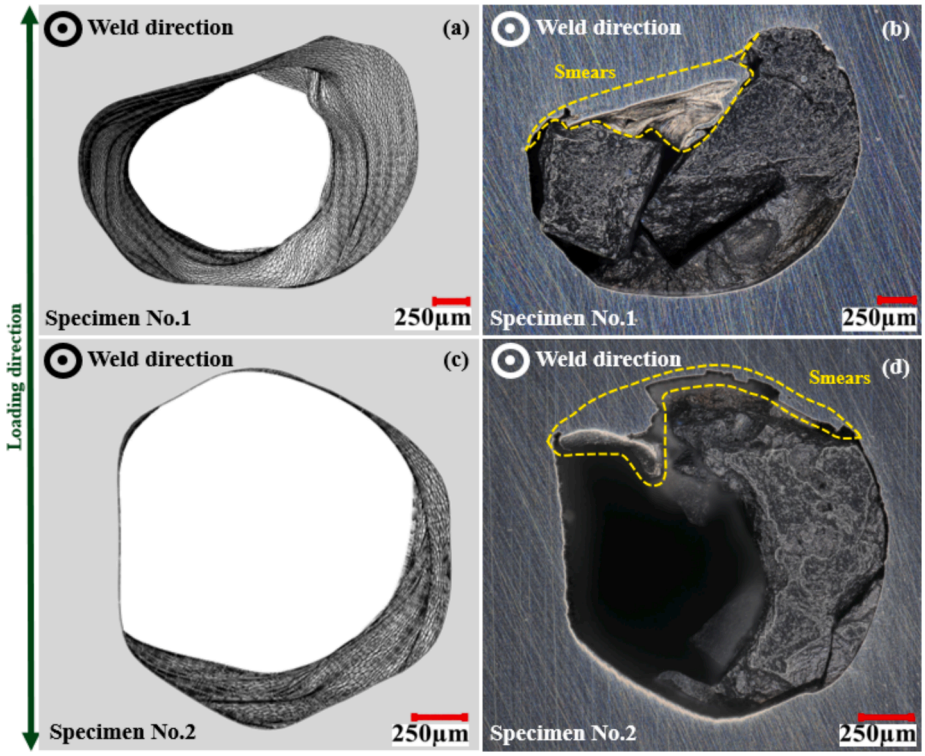


Fig. 5. Comparative analysis of (a) and (c) The actual meshed specimens No.1 and No.2, and (b) and (d) The transverse surfaces of specimens No.1 and No.2 as observed using light microscope.

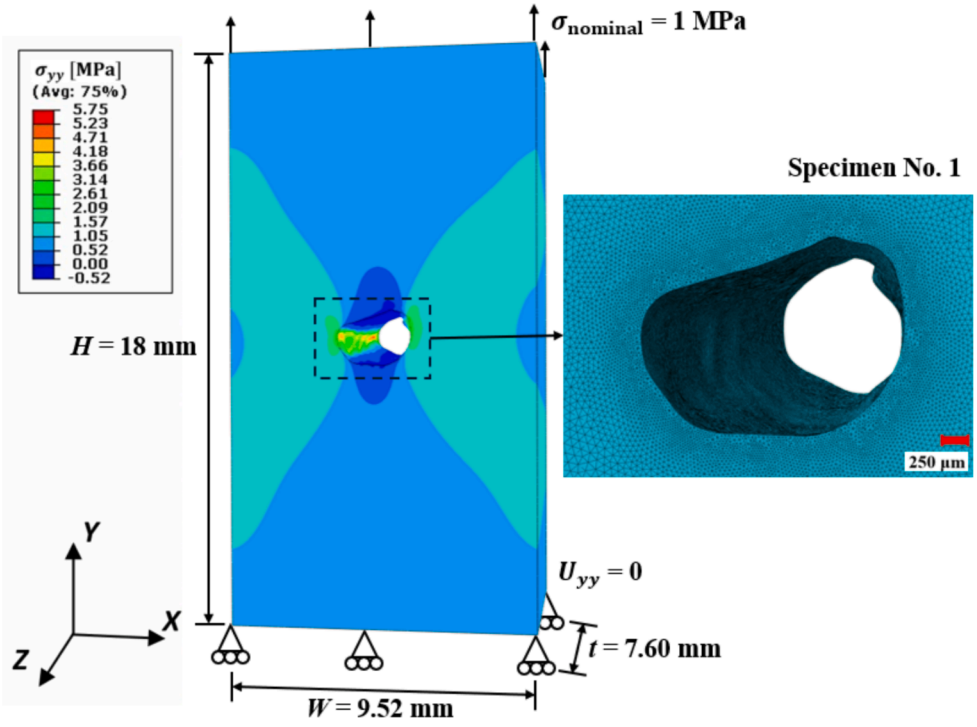


Fig. 6. Finite element stress distribution around the discontinuity of specimen No.1.

finite element analysis (Fig. 8**(b) and (d)**). A comparison of the model with several 2*a* values, measured on the crack surface along the discontinuities, confirms that the discontinuity size was modelled with a precision of 0.06 mm. A specific 2 $a_{(FEA)}$ value was defined for each specimen model. This discontinuity size was measured at the location associated with the Z position where σ_{yy} reaches its maximum, as shown in Fig. 8**(b) and (d)**.

The stress distribution in the crack propagating direction (X direction) was characterized for each fatigue test specimen with the objective of quantifying the singularity exponent. The position along the discon-

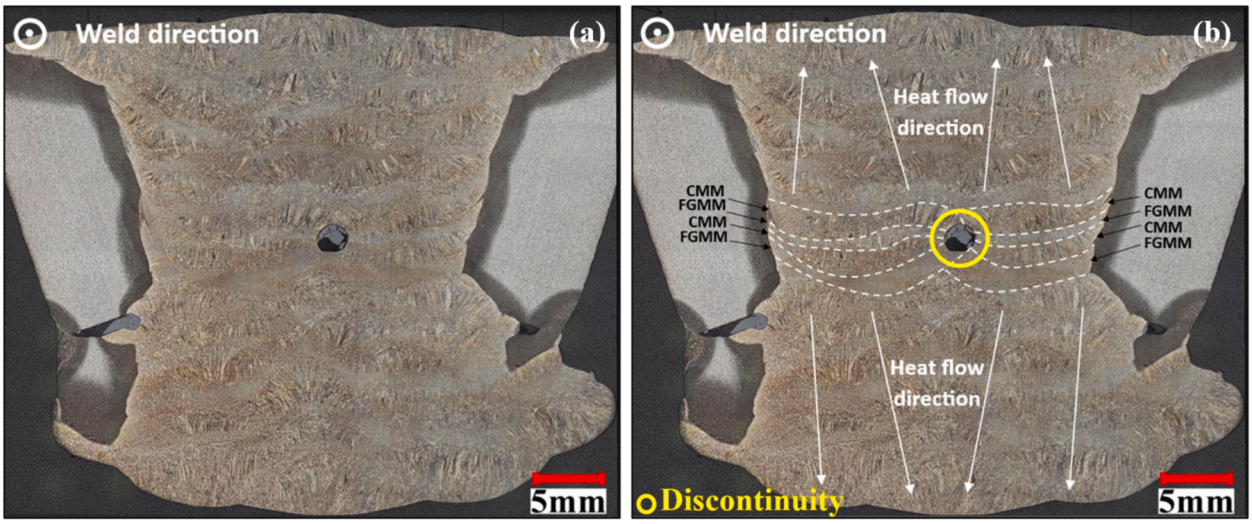


Fig. 7. Distribution of columnar and fine-grained martensitic microstructures in a metallographic sample of a multi-pass weld, PWHT at 605 ± 5 °C for 8 h, etched by Villela. (a) Raw image, (b) Annotated image.

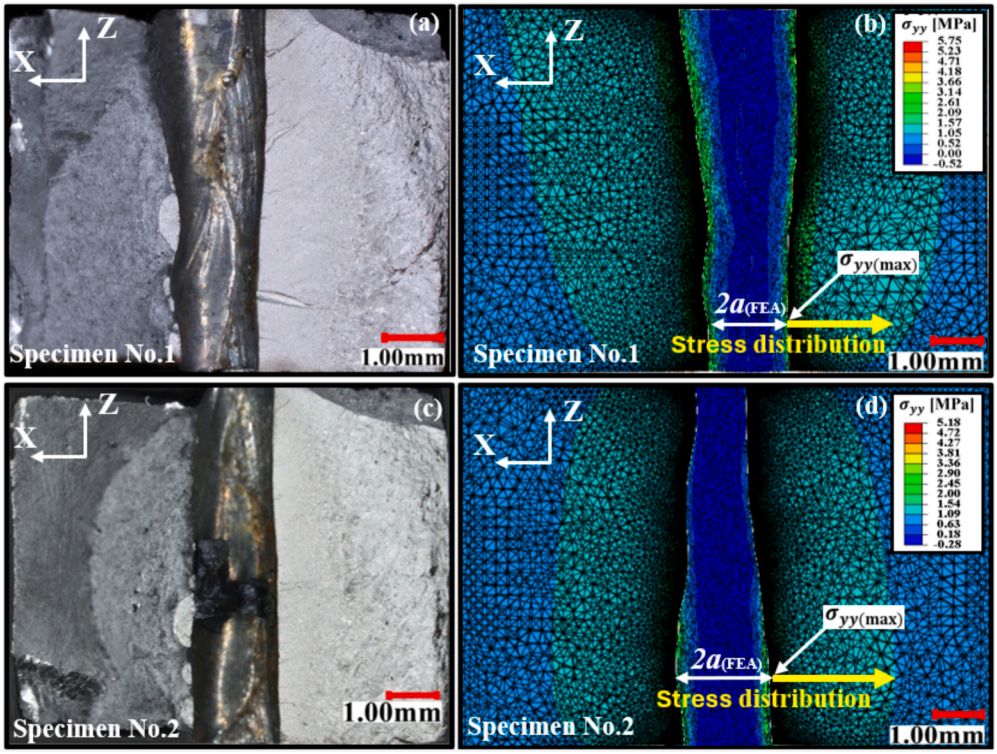


Fig. 8. (a) and (c) Fracture planes of specimens No.1 and No.2 after completing the fatigue test. (b) and (d) Stress distribution on the k_t plane of specimens No.1 and No.2.

tinuity (Z direction) where σ_{yy} is maximum was chosen to perform this characterization. Fig. 9 shows 2 examples of this analysis where the relative stress distribution ($\sigma_{yy}(x)/\sigma_{\text{nominal}}$) is plotted against the relative distance ($x/a_{(\text{FEA})}$) from the root of the discontinuity on a log–log scale.

All elastic stress distributions, characterized between 0.125 $a_{(\text{FEA})}$ and 0.5 $a_{(\text{FEA})}$, follow the power law of **Eq. (2)** as proposed by Verreman et al. [25]:

$$\frac{\sigma_{yy}(x)}{\sigma_{\text{nominal}}} = Y\left(\frac{x}{a_{(\text{FEA})}}\right)^{-\alpha} \tag{2}$$

where Y is the geometrical factor characterizing the discontinuity. The singularity exponent (α) is the slope of the line presented in the graphs of Fig. 9 and the maximum value of $\frac{\sigma_{yy}}{\sigma_{\text{nominal}}}$ is k_t. Fig. 9**(a) and (b)** are two examples of the calculated stress field for specimen No.1 and No.2, respectively. The graphs that describe the other 12 specimens are presented in Fig. S.2 **of** Appendix A – **Supplementary Information**. Williams [26] demonstrated that the singularity of the stress field is a function of the notch opening angle (φ). In this formalism, a crack-like discontinuity ($\varphi \approx 0°$) is characterized by $\alpha = 0.50$ [27] and $Y = 1.00$ for a centered crack in an infinite plate.

To ease interpretation, α, Y, k_t, and $2a_{(\text{FEA})}$ characterizing the stress distributions of each specimen are presented in yellow characters on the

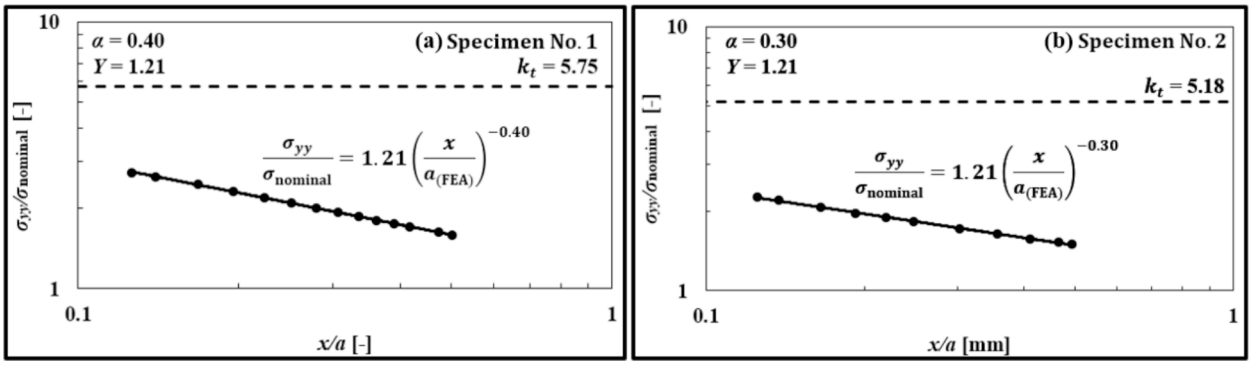


Fig. 9. Normalized stress distribution at the notch tip, bounded by the localized stress concentration factor, k_t. (a) Specimen No.1 and (b) Specimen No.2.

fracture surfaces in Fig. 10. The singularity exponents ranged between 0.27 and 0.45, the geometrical factor ranged between 1.04 and 1.42, and the stress concentration factor varied between 4.06 and 8.31, with one specimen having a much higher k_t of 40.20. This appears to be one scan occurrence where the detection of a small notch was possible. Further metallographic provided in **Section 3.5** supports this hypothesis. The results in Fig. 10 are presented in ascending order of α values, and the fracture surfaces are described in **Section 3.4**.

3.3. Fatigue results

The results of the 14 completed fatigue tests are presented in white characters on Fig. 10. The number of cycles at failure (N_f), the number of steps completed up to $2E^6$ cycles before failure and the fatigue strengths calculated using **Eq. (1)** are reported. It should be noted that the specimen No. 10 failed on the first loading step. The calculated fatigue strength varies between 72 MPa and 171 MPa, with the lowest and highest values obtained for the specimens with the longest and shortest discontinuity, respectively.

3.4. Fractography observations

Fractography observations were performed on the 14 fracture surfaces presented in Fig. 10. For all fatigue test specimens, the fracture planes are normal to the load direction and intersect the artificial discontinuity. Discontinuities were characterized based on their width ($2a$). This parameter was chosen over the $\sqrt{area}$ proposed by Murakami [28] since the discontinuities are wormholes having a length of 7.6 mm. As such, this distinction clearly shows that the discontinuities analyzed here fall outside the size range addressed by Murakami's framework, which is limited to discontinuities up to 1000 μm. Furthermore, the fatigue strength prediction tool must be calibrated to account for the maximum size of each discontinuity to ensure conservative predictions, in accordance with the recommendations of the International Institute of Welding (IIW) [29] for volumetric discontinuities.

The minimum and maximum lengths of the discontinuity ($-2a_{(min)}$ and $2a_{(max)}$) were measured along the X direction on the fracture planes using the Keyence VHX-7000 microscope. Despite the automated welding process, significant variations in the shape of the discontinuity were observed. The smallest and largest values measured across all specimens were 0.18 mm (specimens No.3 and No.4) and 2.94 mm (specimen No.5), respectively.

Failure initiated at multiple sites on each side of the artificial discontinuity, as seen in Fig. 10. A closer examination under SEM of the internal edges, from which most ratchet marks emanate, revealed the presence of a 25 μm thick layer having a grey shade different from the weld material (Fig. 11**(b) and (c)**). EDS performed over this layer indicates a higher concentration of titanium, oxygen, silicon, and zirconium. These findings are consistent with the chemical composition of the flux-cored wire detailed in Table 2, which highlights the significant presence of these elements in the inner flux. Bauné et al. [30] also reported that Ti, Si and Zr are part of the flux-cored electrode's constitutive elements.

On specimens 5, 8, 9, 12, and 13, zones of darker coloration were also observed under optical microscopy. These zones are most likely free surfaces, formed by cold cracking, which would explain why they are covered with oxides produced during the post-weld heat treatment. An EDS elemental mapping performed on specimen No.5 (Fig. 12) showed a much higher concentration of oxygen over this area compared to the filler metal. Elements constituting the flux, such as Ti and Zr, are also present in this region.

3.5. Interrupted fatigue test

A fatigue test was interrupted as soon as a crack was visually detected, allowing for metallographic observations to identify the crack initiation site in the transverse direction. The number of cycles at interruption ($0.95E^6$ cycles) was not a predetermined value. Fig. 13**(a)** shows a crack smaller than 1 mm taking its origin from a region where the radius of curvature of the discontinuity is smaller (sharp corner). The microstructure exposed by etching reveals that the crack initiation is located between two weld beads. Gradual material removal and subsequent observations indicated that the crack was present through the thickness (along the weld direction) and initiated from the sharp corner. Another sharp corner is observed in Fig. 13**(b)**, but no cracks initiated from it. SEM observation using a BSE detector clearly highlighted the initiation site (Fig. 13**(c)**). It is a small notch, corresponding with the step-like feature seen in Fig. 11**(b)**. It measures approximately 25 μm in depth with a radius of about 5 μm. This feature was not captured by the CT scan, as indicated by the superimposed contours in Fig. 13**(b)**. The stress concentration factor characterizing this small feature is much higher than that predicted by FEA. The microstructure in the crack propagation area is a fine martensite with no particularities worth mentioning.

4. Prediction of the fatigue resistance

The general objective of this work is to apply the generalized Atzori-Lazzarin approach using the LENM to predict the fatigue strength of the tested specimens. The LEFM and LENM equations used to anticipate the effect of a discontinuity, having a length a, on the fatigue strength of a material, $\Delta\sigma$, are very similar, as shown by **Eqs. (3)** and **(4)**. Two aspects differentiate **Eqs. (3)** and **(4)**. The former is based on a stress distribution that evolves with a singularity exponent of 0.5, while LENM is generalized to any stress distribution characterized by a singularity exponent α. LEFM predicts that a crack will propagate to failure if the critical stress intensity factor range reaches the long crack threshold (ΔK_{th}), while LENM predicts crack propagation based on notch-specific thresholds ($\Delta K_{th,n}$). Overall, LEFM is a specific case of LENM with $\alpha = 0.5$ and $\Delta K_{th,n} = \Delta K_{th}$.



Fig. 10. Fracture planes of the fatigue specimens annotated with corresponding FEA and fatigue test results. The multi-pass weld is oriented in the X direction: root on the right, covering zone on the left side of the discontinuities. The loading direction is orthogonal to the observed planes. The results are presented in ascending order of the singularity exponent, α.

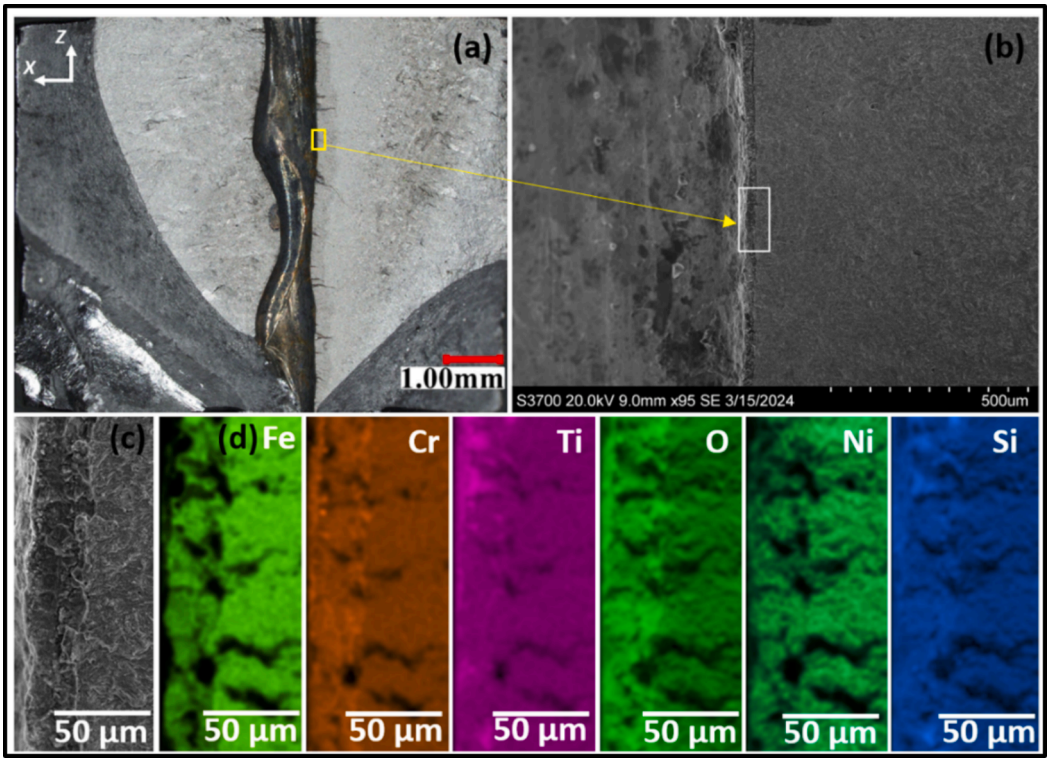


Fig. 11. Analyses of fracture surfaces in welded specimen No. 8: (a) Overview with light microscope, (b) High-resolution SEM image, (c) SEM detail of ratchet marks at the weld root and (d) EDS elemental mapping (white rectangle). The multi-pass weld is oriented in the X direction: root on the right, covering zone on the left side of the discontinuities.

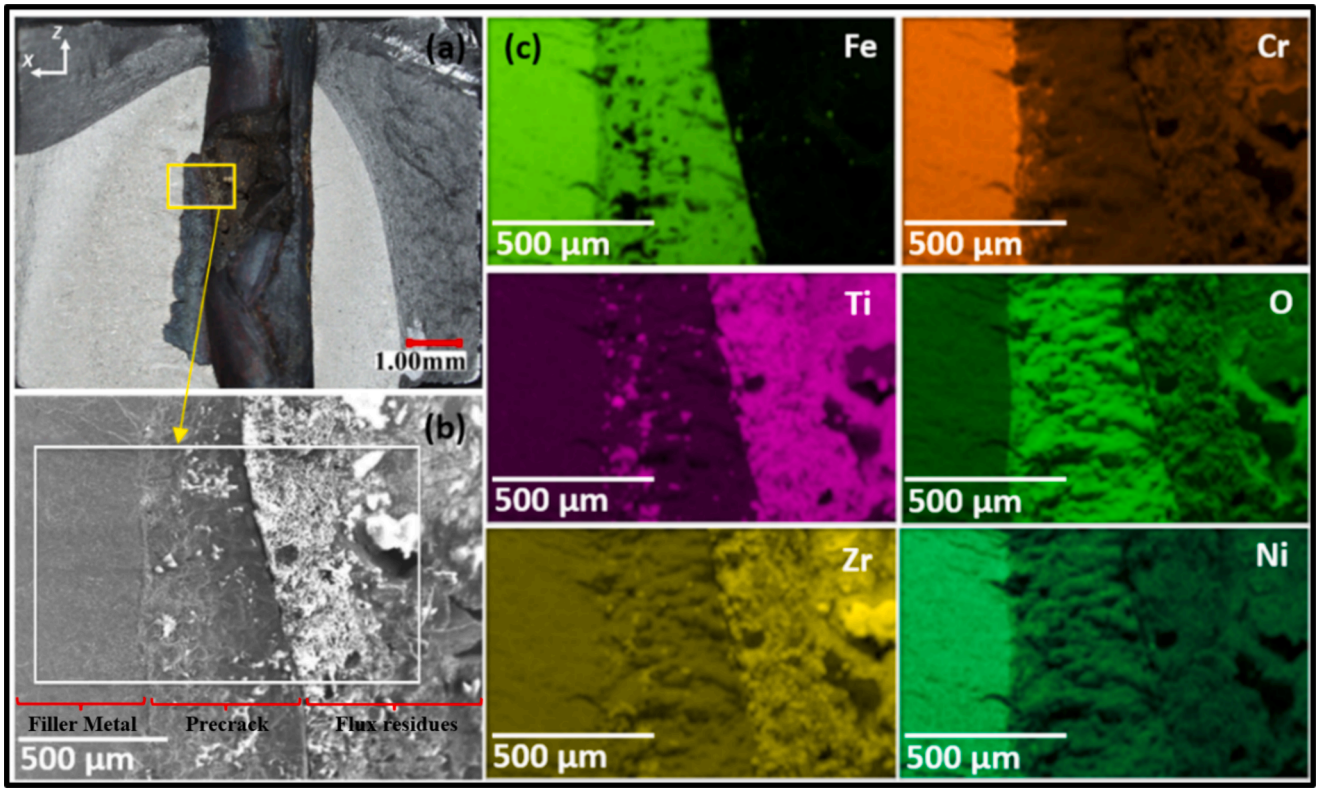


Fig. 12. Analyses of fracture surfaces in welded specimen No.5: (a) Overview with light microscope, (b) SEM detail, and (c) EDS elemental mapping (white rectangle). The multi-pass weld is oriented in the X direction: root on the right, covering zone on the left side of the discontinuities.

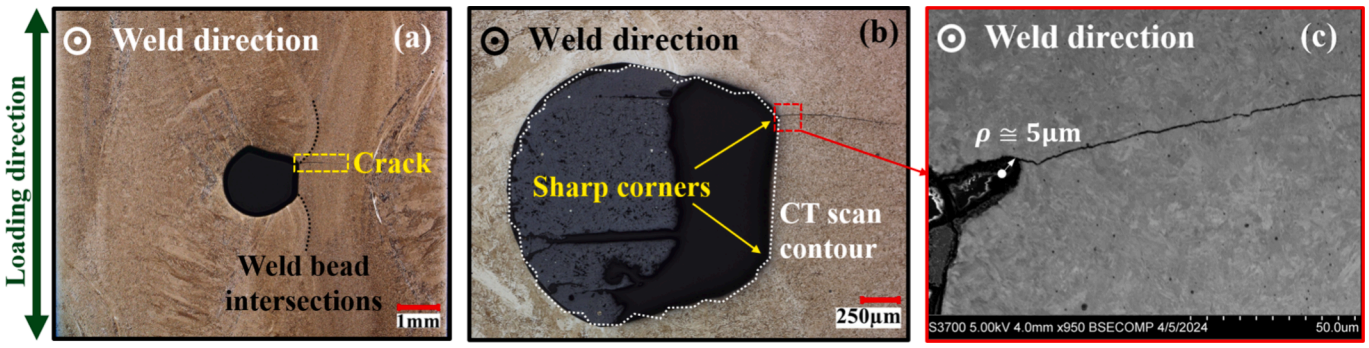


Fig. 13. Light microscope images of crack initiation: (a) Overview from the weld root and (b) Zoomed-in view with CT scan contour superimposed. (c) BSE image showing crack initiation from a small notch. The sample was etched by Villela. The multi-pass weld is oriented in the X direction: root on the right, covering zone on the left side of the discontinuities.

$$\Delta\sigma_{\mathrm{LEFM}} = \frac{\Delta K_{\mathrm{th}}}{Y\sqrt{\pi a}} \tag{3}$$

$$\Delta\sigma_{\mathrm{LENM}} = \frac{\Delta K_{\mathrm{th,n}}}{Y\sqrt{\pi}a^{\alpha}} \tag{4}$$

When plotted on a graph with the logarithm of discontinuity size and the logarithm of the stress variation as the axes, **Eqs. (3)** and **(4)** are straight lines with slopes of -0.5 and $-\alpha$, respectively.

In the Atzori-Lazzarin (AL) diagram, the fatigue strength values of a smooth and notch specimens ($\Delta\sigma_0$ and $\Delta\sigma_0/k_t$) represent the upper and lower bounds of LENM, respectively. These values define the limits within which LENM is applicable. The discontinuity size at the intersection point of the LENM with the upper bound is commonly referred to as $a_{0,n}$. This parameter is analogous to the El Haddad-Smith-Topper parameter (a_0) [31], which defines the upper bound of application for LEFM. The values of $a_{0,n}$ can be calculated by equating $\Delta\sigma_{\mathrm{LENM}} = \Delta\sigma_0$ as proposed in **Equation 5**. The discontinuity size at the lower bound of LENM is referred to as a_n^*. It is obtained by equating $\Delta\sigma_{\mathrm{LENM}} = \Delta\sigma_0$ as shown in **Equation 6**.

$$a_{0,n} = \left(\frac{\Delta K_{\mathrm{th,n}}}{Y\sqrt{\pi}\,\Delta\sigma_0}\right)^{\frac{1}{\alpha}} \tag{5}$$

$$a_n^* = a_{0,n}k_t^{\frac{1}{\alpha}} \tag{6}$$

The threshold stress intensity factor range of a notch, $\Delta K_{\mathrm{th,n}}$, combines material properties and notch characteristics. Atzori et al. [10] proposed the following equation to relate $\Delta K_{\mathrm{th,n}}$ with ΔK_{th} and α based on the notch stress intensity factor (NSIF) theory:

$$\Delta K_{\mathrm{th,n}} = \beta(\Delta\sigma_0)^{(1-2\alpha)}\Delta K_{\mathrm{th}}{}^{2\alpha} \tag{7}$$

where β is a dimensionless parameter. Atzori et al. [11] proposed to use the point method (PM) to calculate β_{PM} using **Equation 8**:

$$\beta_{PM} = \frac{\sqrt{2}}{2^{\alpha}}\pi^{((1/2)-\alpha)} \tag{8}$$

To complete the AL diagram of each specimen under study, $\Delta K_{\mathrm{th,n}}$, was calculated by combining **Eqs. (7)** and **(8)**. The α calculated by the FEA and a ΔK_{th} value of 5.16 MPa $\sqrt{\mathrm{m}}$ were used for the calculation. This latter value was experimentally measured by Patriarca et al. [32] for the same 410NiMo welded material. Details of $\Delta K_{\mathrm{th,n}}$ calculation using information from Table S.1, including ΔK_{th} and $\Delta\sigma_0$ values, are presented in Section S2 **of** Appendix A – **Supplementary Information**.

Fig. 15 **(a) and (b)** show the LEFM (blue line) and LENM (black line) theories applied to specimens No.1 and No.2, respectively. The red point with the horizontal bar represents the experimental fatigue strength reported over the discontinuity size range measured on the fracture surfaces. The point is positioned at $a_{(\mathrm{mean})} = (a_{(\mathrm{min})} + a_{(\mathrm{max})})/2$.

The specimens chosen for the examples given in Fig. 14 have singularity exponents of 0.40 and 0.30, respectively. The graphs that describe the other specimens are presented in Fig. S.3 **of** Appendix A – **Supplementary Information**. Independently of the singularity exponent, the LEFM seems to better predict the fatigue strength of most specimens, as shown in Fig. 15.

Fig. 15 is used to correlate the fatigue strength predictions given by the LEFM and LENM approaches with all the experimental results. The Y-axis represents the predicted values, while the X-axis represents the experimental values. Each experimental results is presented by two data points, one triangle and one square. The triangle and the square correspond to ($\Delta\sigma_{\mathrm{LENM}}$, $\Delta\sigma_{\mathrm{exp}}$) and ($\Delta\sigma_{\mathrm{LEFM}}$, $\Delta\sigma_{\mathrm{exp}}$), respectively. Both the triangle and square data points are reported for the specific $a_{(\mathrm{max})}$ of each specimen. The black dashed line represents the ideal prediction model where predictions perfectly match the experimental results (slope of 1). All data reported above and below this line are overestimating and underestimating the experiment results, respectively.

Out of the 14 specimens, 13 had overestimated fatigue strength predictions when using the LENM, whereas the fatigue strength of only one specimen was overestimated when using the LEFM.

The Mean Absolute Percentage Error (MAPE) and the Relative Standard Deviation (RSD) were calculated by comparing the experimental data to the ideal prediction model. The MAPE characterizing the LEFM and LENM predictions are 16.1 % and 33.7 %, respectively. Therefore, the prediction accuracy (calculated as 100 – MAPE) is 83.9 % for LEFM and 66.3 % for LENM, with associated RSD values of 14.4 % and 34.0 %, reflecting the variability in the prediction errors.

Since LEFM led to the most accurate fatigue strength prediction, its application was further explored. The discontinuity size variation through the specimen thickness and the existence of multiple crack initiation sites triggered a question. What discontinuity size parameter between $a_{(\mathrm{min})}$, $a_{(\mathrm{max})}$ and $a_{(\mathrm{mean})}$ will lead to the most accurate fatigue strength predictions?

Fig. 16**(a) and (b)** present the experimental results in a KT diagram. In Fig. 16**(a),** the fatigue strength is reported over the average size of the discontinuities $a_{(\mathrm{mean})}$, while in Fig. 16**(b),** bands spanning the $a_{(\mathrm{min})}$ and $a_{(\mathrm{max})}$ values are presented. These comparative graphs reveal that the LEFM predictions provide a good estimation of the fatigue strength related to the average discontinuity size measured on the fracture surfaces. Additionally, for most specimens, conservative fatigue strength predictions can be obtained using $a_{(\mathrm{max})}$.

Based on the ΔK_{th} and $\Delta\sigma_0$ parameters used in this study, the El Haddad-Smith-Topper parameter (a_0) [31] is 0.031 mm for the 410NiMo welded material.

5. Discussion

The primary objective of this research work was to predict the

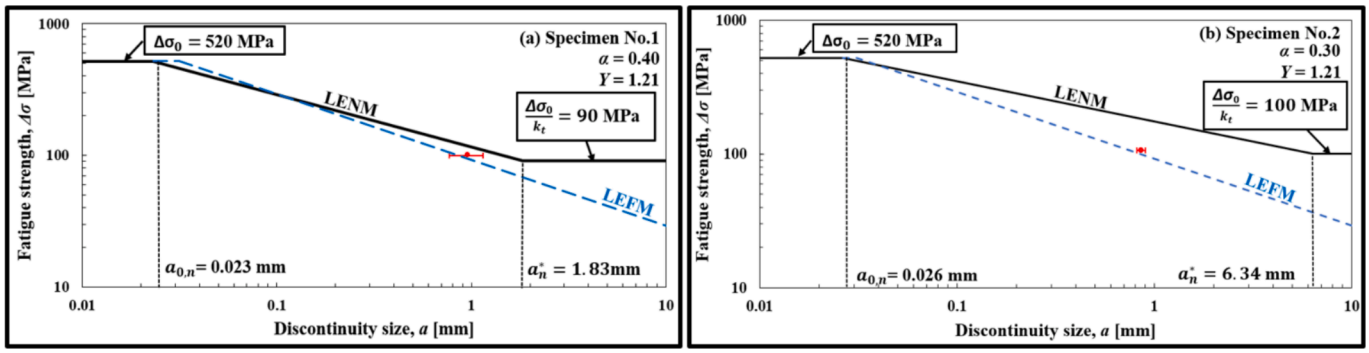


Fig. 14. Fatigue strength of elongated discontinuities in the 410NiMo welded material for $N = 2E^6$ cycles and $R = 0.1$. Predictions from (black line) Notch theory, (blue line) Linear elastic fracture mechanics and (red bar) Experimental data. (a) Specimen No.1 and (b) Specimen No.2.

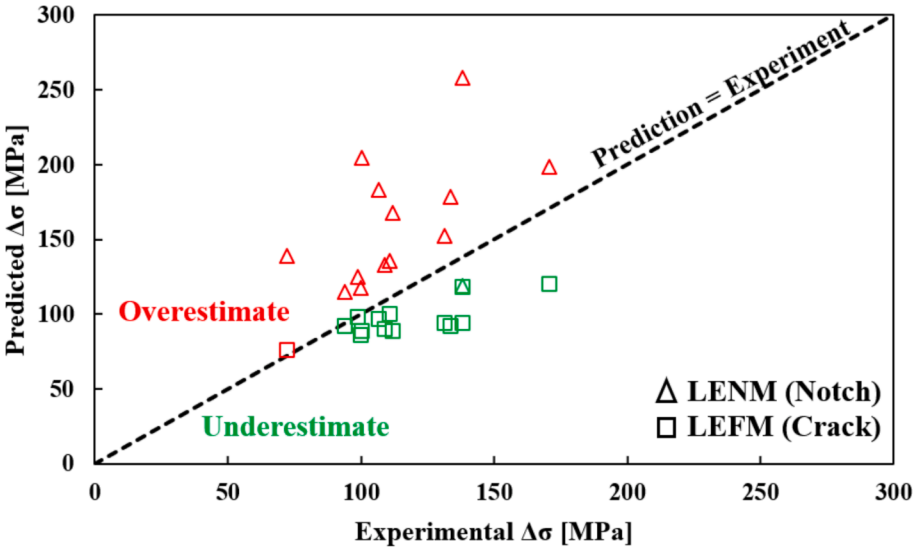


Fig. 15. Fatigue strength comparison using LEFM and LENM approaches using maximum discontinuity size.

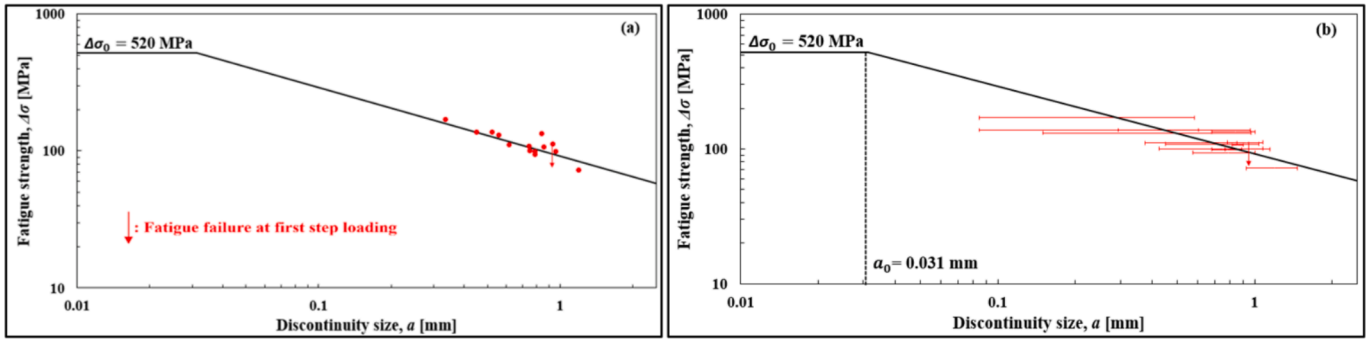


Fig. 16. Results on the Kitagawa-Takahashi diagram showing (a) Mean discontinuity size, and (b) Discontinuity size variation. The red arrow indicates the applied stress variation that led to the fatigue failure of specimen No.10 during the first loading step.

fatigue resistance of welds containing wormlike discontinuities ranging from 0.18 mm to 2.94 mm. These discontinuities were successfully introduced by adding flux residue between weld beads. This study focused on 410NiMo weld metal; a material widely used in hydroelectric turbines but insufficiently studied in terms of fatigue behavior. The goal was to bridge this knowledge gap through experimental validation and numerical modelling to assess the impact of complex volumetric discontinuities on fatigue strength.

The application of notch theory, calibrated with the singularity exponent characterizing the local stress field predicted by finite element simulation, was unable to improve the accuracy of the fatigue strength predictions under the studied conditions. Several explanations can be proposed.

While the surrogate discontinuities have mesoscale dimensions on the millimeter scale and are detectable by CT scans, microscopic heterogeneities at the micron scale remain undetectable. The finite element simulations were performed using the geometry of discontinuities characterized by CT scans with a resolution of 20 μm/voxel. Patterson

et al. [33] reported that detail detectability of a CT scan is typically 3 times the voxel size. Considering that the crack-initiating discontinuity shown in Fig. 13**(c)** has a length smaller than 60 μm, this notch was not revealed by the CT scan and, therefore, was not accounted for in the numerical simulation of the stress field. This explains why the singularity exponent calculated by FEA is less than 0.5 for all studied specimens. At the tip of the micro-notch, the singularity exponent is probably closer to 0.5, as the angle between the notch lips approaches zero. This inability to capture fine-scale features may lead to inaccuracies in modelling the local stress field and, consequently, fatigue strength predictions. However, one specimen characterized by the k_t of 40.20 had a better geometrical definition, suggesting a successful detection of the micro-notch.

In addition to the notch-like discontinuities, 5 out of the 14 specimens suffered from cracking prior to fatigue testing. The oxide present on a portion of the fractured surface indicates that small cracks, ranging from 50 μm to 700 μm in depth, existed before the post-weld heat treatment was performed. These cracks were not revealed by the CT scan.

Another notable observation from EDS analysis performed on the fractured surface is the high concentration of elements belonging to the flux. Ti, Si and Zr were highly concentrated at the crack initiation sites, particularly in the oxidized regions (notch surfaces and pre-crack areas). Even though no characterization of their embrittlement potential was performed, the diffusion of foreign elements into the filler material is often undesirable, as it has the potential to modify the material's resistance to crack initiation and propagation. ASME standards [34] have indicated that the presence of flux residues can be extremely corrosive, and certain researchers have highlighted the harmful effects of these elements [4,35].

After studying the fractured surfaces and comparing the fatigue results with analytical fatigue strength predictions performed with LENM and LEFM, several observations were made:

1) Welding discontinuities introduced in a controlled environment suggest that their impact on fatigue strength is similar to that of crack-like discontinuities for the following reasons:

- Small notches, undetected by CT scan, are produced at the superposition of weld beads; these notches may have a singularity exponent closer to 0.5.
- Cracks, undetected by CT scan, are prone to form during welding; these cracks have a singularity exponent of 0.5.

2) Foreign elements belonging to flux residues were found at crack initiation sites. Their presence can embrittle the material.

Compared to previous studies on welded joints with standard discontinuities by Atzori and others [13–15], this study extends the understanding of volumetric complex discontinuities, demonstrating that notch-based fatigue strength predictions may not be directly applicable to such flaws. Applying the LENM proves to be unsafe for the durability of turbine runners, as the calculated inspection intervals may lead to unexpected risks. This research empirically validates that the discontinuities introduced in the weld are crack-like discontinuities. Hydro-Québec's current approach used to predict the operational fatigue life of hydraulic turbines is substantiated by this research. In industrial applications, slag-related discontinuities are typically not characterized with the level of detail necessary to fully benefit from the NSIF approach.

6. Conclusion

This research introduces advanced methodologies for the fatigue strength prediction of 410NiMo welds with surrogate discontinuities, characterized using high-resolution CT scans, and addresses significant gaps in the existing literature. The primary contributions of this study are as follows:

Controlled introduction of discontinuities

- Realistic wormlike slag inclusions (0.18 mm to 2.94 mm) were introduced as surrogate discontinuities via robotic welding.
- These inclusions replicate flaws typically associated with the FCAW process.

CT-based characterization

- A high-resolution CT scan (20 μm/voxel) was used to characterize discontinuities.
- This provided detailed geometric insight, enabling precise finite element analysis of stress distributions.

Validation of notch stress intensity factor (NSIF) for volumetric discontinuities

- The applicability of NSIF for slag-type discontinuities in welded 410NiMo components demonstrates its limitations in fatigue strength prediction compared to LEFM.

Fatigue strength prediction accuracy

- The fatigue strength of the specimens at $R = 0.1$ and $2E^6$ cycles ranged between 72 MPa and 171 MPa.
- The stress singularity exponents ranged from 0.27 to 0.45, which is lower than the 0.5 exponent characterizing a crack.

7. Recommendation

Volumetric discontinuities from welding should be treated as crack-like discontinuities, as proposed by the ASME standards [34]. The Kitagawa-Takahashi diagram (based on the maximum defect width) is recommended for predicting the fatigue strength of elongated wormlike discontinuities, as it provides a prediction accuracy of 83.9 ± 14.4 % when accounting for the maximum discontinuity size.

CRediT authorship contribution statement

C. Constantineau: Writing – review & editing, Writing – original draft, Visualization, Software, Methodology, Investigation, Formal analysis, Data curation, Conceptualization. **P.A. Deschênes:** Writing – review & editing, Validation, Supervision, Resources, Project administration, Methodology, Investigation, Conceptualization. **R. Dubois:** Methodology. **M. Brochu:** Writing – review & editing, Validation, Supervision, Resources, Project administration, Investigation, Funding acquisition, Conceptualization.

Declaration of competing interest

The authors declare that they have no known competing financial interests or personal relationships that could have appeared to influence the work reported in this paper.

Acknowledgements

This work was supported by the Hydro-Québec Research Institute (IREQ), the Consortium de recherche et d'innovation en transformation métallique (CRITM), the National Sciences and Engineering Research Council of Canada (NSERC) and the Mathematics of Information Technology and Complex Systems (MITACS). The help of technologists Alexandre Lapointe, Alexandre Tremblay, Carlo Baillargeon, Jimmy Pichette and René Dubois from Hydro-Québec is gratefully acknowledged.

Appendix A. Supplementary data

Supplementary data to this article can be found online at https://doi.org/10.1016/j.ijfatigue.2025.108955.

Data availability

Data will be made available on request.

References

[1] Amrei M, Monajati H, Thibault D, Verreman Y, Bocher P. Effects of various post-weld heat treatments on austenite and carbide formation in a 13Cr4Ni steel multipass weld. Metall Microstruct Anal 2016;5(1):50–61. https://doi.org/10.1007/s13632-015-0251-z.

[2] Amrei M. Characterization of microstructure and texture of 13Cr4Ni martensitic stainless steel weld before and after tempering. Montréal: École de technologie supérieure; 2016.

[3] D'Andrea A, Gagnon M, Beretta S, Bocher P. Measurements and prediction of extreme defect distributions for fatigue assessment in multi-pass weld of 13% Cr–4% Ni alloy for hydraulic turbines. Int J Fatigue 2024;188:108501.

[4] Habibzadeh Boukani H, Viens M, Tahan S-A, Gagnon M. Case study on the integrity and nondestructive inspection of flux-cored arc welded joints of Francis turbine runners. Int J Adv Manuf Technol 2018;98(5–8):2201–11. https://doi.org/10.1007/s00170-018-2139-y.

[5] Gagnon M, Tahan A, Bocher P, Thibault D. On the fatigue reliability of hydroelectric francis runners. Procedia Eng 2013;66:565–74. https://doi.org/10.1016/j.proeng.2013.12.108.

[6] Thibault D, Gagnon M, Godin S. The effect of materials properties on the reliability of hydraulic turbine runners. Int J Fluid Mach Syst 2015;8(4):254–63. https://doi.org/10.5293/ijfms.2015.8.4.254.

[7] Kitagawa H. Applicability of fracture mechanics to very small cracks or the cracks in the early stage. In: Proc. 2nd int. conf. on mechanical behaviour of materials; 1976. p. 627–31.

[8] Meimandi S. Characterization of shrinkage porosity and fatigue properties of cast CA-6NM low carbon martensitic stainless steels," École de technologie supérieure; 2021.

[9] Akbarian F. Influence of the Discontinuities on the Fatigue Behavior of Welded 410NiMo Turbines. Montréal: Mémoire, Génie mécanique, École polytechnique de Montréal; 2023.

[10] Atzori B, Lazzarin P, Meneghetti G. A unifying approach to fatigue design in presence of defects and notches subject to uniaxial loading. In: MATEC Web of Conferences, 2014, vol. 12: EDP Sciences, p. 09001.

[11] Atzori B, Lazzarin P, Meneghetti G. A unified treatment of the mode I fatigue limit of components containing notches or defects. Int J Fract 2005;133:61–87.

[12] Ghafoori-Ahangar R, Verreman Y. Fatigue behavior of load-carrying cruciform joints with partial penetration fillet welds under three-point bending. Eng Fract Mech 2019;215:211–23. https://doi.org/10.1016/j.engfracmech.2019.05.015.

[13] Atzori B, Meneghetti G, Susmel L. Estimation of the fatigue strength of light alloy welds by an equivalent notch stress analysis. *Int J Fatigue* 2002;24(5):591–9.

[14] Atzori B, Lazzarin P, Meneghetti G. Fatigue strength assessment of welded joints: From the integration of Paris' law to a synthesis based on the notch stress intensity factors of the uncracked geometries. *Eng Fract Mech* 2008;75(3–4):364–78. https://doi.org/10.1016/j.engfracmech.2007.03.029.

[15] Al Zamzami I, Susmel L. On the accuracy of nominal, structural, and local stress based approaches in designing aluminium welded joints against fatigue. *Int J Fatigue* 2017;101:137–58. https://doi.org/10.1016/j.ijfatigue.2016.11.002.

[16] Schuscha M, Horvath M, Leitner M, Stoschka M. Notch stress intensity factor (NSIF)-based fatigue design to assess cast steel porosity and related artificially generated imperfections. *Metals* 2019;9(10):1097. https://doi.org/10.3390/met9101097.

[17] Consonni M, Wee CF, Schneider C. Manufacturing of welded joints with realistic defects. *Insight-Non-Destructive Testing and Condition Monitoring* 2012;54(2):76–81.

[18] Trudel A, Sabourin M, Lévesque M, Brochu M. Fatigue crack growth in the heat affected zone of a hydraulic turbine runner weld. *Int J Fatigue* 2014;66:39–46.

[19] ASTM A5.22/A5.22M. Specification for Stainless Steel Flux Cored and Metal Cored Welding Electrodes and Rods; 2020.

[20] Yoon CS, Paik NW, Kim JH, Chae HB. Total and soluble metal contents in flux-cored arc welding fumes. *Aerosol Sci Tech* May 2009;43(6):511–21. https://doi.org/10.1080/02786820902773669.

[21] ASTM E466. Standard Practice for Conducting Force Controlled Constant Amplitude Axial Fatigue Tests of Metallic Materials; 2021.

[22] ASTM E407. Standard Practice for Microetching Metals and Alloys; 2015.

[23] Locati L. Le prove di fatica come ausilio alla progettazione ed alla produzione. Metall Ital 1955;47(9):301–8.

[24] Maxwell DC, Nicholas T. A rapid method for generation of a Haigh diagram for high cycle fatigue. *Fatigue and Fracture Mechanics: 29th Volume*. ASTM International; 1999.

[25] Verreman Y, Limodin N. Fatigue notch factor and short crack propagation. Eng Fract Mech 2008;75(6):1320–35. https://doi.org/10.1016/j.engfracmech.2007.07.005.

[26] Williams ML. Stress singularities resulting from various boundary conditions in angular corners of plates in extension. J Appl Mech, 1952;19(4):526–8.

[27] Irwin GR. Analysis of stresses and strains near the end of a crack traversing a plate. J Appl Mech, 1957;24:361–4.

[28] Murakami Y, Beretta S. Small defects and inhomogeneities in fatigue strength: experiments, models and statistical implications. *Extremes* Jun. 1999;2:123–47.

[29] Hobbacher AF, Baumgartner J. Recommendations for Fatigue Design of Welded Joints and Components, 3rd ed., IIW Collection. Cham, Switzerland: Springer, 2024. doi: 10.1007/978-3-031-57667-6.

[30] Bauné E, Bonnet C, Liu S. Reconsidering the basicity of a FCAW consumable-part 1: solidified slag composition of a FCAW consumable as a basicity indicator. Welding Journal-New York 2000;79(3). pp. 57-s.

[31] El Haddad MH, Topper TH, Smith KN. Prediction of non propagating cracks. Eng Fract Mech 1979;11(3):573–84. https://doi.org/10.1016/0013-7944(79)90081-x.

[32] Patriarca L, D'Andrea A, Cova M, Rusnati L, Beretta S. Cyclic r-curve measurements for structural metallic alloys. Adv Eng Mater 2024;26(19):2400447. https://doi.org/10.1002/adem.202400447.

[33] Patterson BM, Escobedo-Diaz JP, Dennis-Koller D, Cerreta E. Dimensional quantification of embedded voids or objects in three dimensions using X-ray tomography. Microsc Microanal 2012;18(2):390–8.

[34] Section VIII - Rules for Construction of Pressure Vessels Division 1, A. BPVC; 2017.

[35] Quintana M, McLane J, Babu S, David S. Inclusion formation in self-shielded flux cored arc welds. Welding Journal-New York 2001;80(4):98S–105S.